

See discussions, stats, and author profiles for this publication at: <https://www.researchgate.net/publication/8689225>

# Single-Molecule Magnets: A Large $Mn_3O$ Molecular Nanomagnet Exhibiting Quantum Tunneling of Magnetization

ARTICLE in JOURNAL OF THE AMERICAN CHEMICAL SOCIETY · MARCH 2004

Impact Factor: 12.11 · DOI: 10.1021/ja0297638 · Source: PubMed

CITATIONS

215

READS

32

## 5 AUTHORS, INCLUDING:



Monica Soler

University of Chile

36 PUBLICATIONS 1,386 CITATIONS

SEE PROFILE



Wolfgang Wernsdorfer

French National Centre for Scientific Research

611 PUBLICATIONS 31,884 CITATIONS

SEE PROFILE



George Christou

University of Florida

757 PUBLICATIONS 28,963 CITATIONS

SEE PROFILE

# Single-Molecule Magnets: A Large $\text{Mn}_{30}$ Molecular Nanomagnet Exhibiting Quantum Tunneling of Magnetization

Monica Soler,<sup>†</sup> Wolfgang Wernsdorfer,<sup>‡</sup> Kirsten Folting,<sup>§</sup> Maren Pink,<sup>§</sup> and George Christou<sup>\*,†</sup>

*Contribution from the Department of Chemistry, University of Florida, Gainesville, Florida 32611-7200, Laboratoire Louis Néel-CNRS, BP 166, 25 Avenue des Martyrs, 38042 Grenoble, Cedex 9, France, and Molecular Structure Center, Indiana University, Bloomington, Indiana 47405-7102*

Received December 16, 2002; E-mail: christou@chem.ufl.edu

**Abstract:** The largest single-molecule magnet (SMM) to date has been prepared and studied. Recrystallization of known  $[\text{Mn}_{12}\text{O}_{12}(\text{O}_2\text{CCH}_2\text{Bu})_{16}(\text{H}_2\text{O})_4]$  (**1**;  $8\text{Mn}^{\text{III}}$ ,  $4\text{Mn}^{\text{IV}}$ ) from  $\text{CH}_2\text{Cl}_2/\text{MeNO}_2$  causes its conversion to  $[\text{Mn}_{30}\text{O}_{24}(\text{OH})_8(\text{O}_2\text{CCH}_2\text{Bu})_{32}(\text{H}_2\text{O})_2(\text{MeNO}_2)_4]$  (**2**;  $3\text{Mn}^{\text{II}}$ ,  $26\text{Mn}^{\text{III}}$ ,  $\text{Mn}^{\text{IV}}$ ). The structure of **2** consists of a central, near-linear  $[\text{Mn}_4\text{O}_6]$  backbone, to either side of which are attached two  $[\text{Mn}_{13}\text{O}_9(\text{OH})_4]$  units. Peripheral ligation around the resulting  $[\text{Mn}_{30}\text{O}_{24}(\text{OH})_8]$  core is by 32  $\text{Bu}'\text{CH}_2\text{CO}_2^-$ , 2  $\text{H}_2\text{O}$ , and 4  $\text{MeNO}_2$  groups. The molecule has crystallographically imposed  $C_2$  symmetry. Variable-temperature and -field magnetization ( $M$ ) data were collected in the 1.8–4.0 K and 0.1–0.4 T ranges and fit by matrix diagonalization assuming only the ground state is occupied at these temperatures. The fit parameters were  $S = 5$ ,  $D = -0.51 \text{ cm}^{-1} = -0.73 \text{ K}$ , and  $g = 2.00$ , where  $D$  is the axial zero-field splitting parameter. AC susceptibility measurements in the 1.8–7.0 K range in a zero DC field and a 3.5 G AC field oscillating at frequencies in the 50–997 Hz range revealed a frequency-dependent out-of-phase ( $\chi''$ ) signal below 3 K, indicating **2** to be a single-molecule magnet (SMM), the largest yet obtained. Magnetization versus DC field sweeps show hysteresis loops but no clear steps characteristic of quantum tunneling of magnetization (QTM). However, magnetization decay data below 1 K were collected and used to construct an Arrhenius plot that revealed temperature-independent relaxation below 0.3 K. The fit of the thermally activated region above  $\sim 0.5 \text{ K}$  gave  $U_{\text{eff}}/k = 15 \text{ K}$ , where  $U_{\text{eff}}$  is the effective relaxation barrier. Resonant QTM was confirmed from the appearance of a “quantum hole” when the recent quantum hole digging method was employed. The combined results demonstrate that SMMs can be prepared that are significantly larger than any known to date and that this new, large  $\text{Mn}_{30}$  complex still demonstrates quantum behavior.

## Introduction

The interface between classical and quantum science is a fascinating area that has been the focus of a great deal of study for many decades. Even so, there has been a surge of interest in this area in recent years as a result of the current explosive thrusts in nanoscience, because taking devices to the limit of miniaturization (the nanoscale and beyond) means that quantum effects become important. It thus becomes essential to understand the interplay, at this intermediate or mesoscale, between the classical properties of the macroscale and the quantum properties of the microscale. This is particularly true in nanomagnetism, where many potential applications require monodisperse, magnetic nanoparticles. One important source of such species are single-molecule magnets (SMMs),<sup>1–5</sup> individual molecules that function as single-domain magnetic particles of

nanoscale (and even subnanoscale) dimensions. Thus, SMMs exhibit the superparamagnetic-like properties normally observed with much larger particles of common magnetic materials such as Co metal, iron oxides, etc. As a result, below their blocking temperature ( $T_B$ ), they exhibit magnetization hysteresis, the classical macroscale property of a magnet, as well as quantum tunneling of magnetization (QTM)<sup>6,7</sup> and quantum phase interference,<sup>8</sup> the properties of a microscale entity.

SMMs represent a molecular or “bottom-up” approach to nanoscale magnets, and they thus possess many advantages over normal magnetic materials in this size range. These include monodispersity, ordered assemblies within crystals, true solubility (rather than colloidal suspension) in organic solvents, and

<sup>†</sup> University of Florida.

<sup>‡</sup> Laboratoire Louis Néel.

<sup>§</sup> Indiana University.

- (1) Christou, G.; Gatteschi, D.; Hendrickson, D. N.; Sessoli, R. *MRS Bull.* **2000**, 25, 66.
- (2) Sessoli, R.; Ysaï, H.-L.; Schake, A. R.; Wang, S.; Vincent, J. B.; Folting, K.; Gatteschi, D.; Christou, G.; Hendrickson, D. N. *J. Am. Chem. Soc.* **1993**, 115, 1804.

- (3) Sessoli, R.; Gatteschi, D.; Caneschi, A.; Novak, M. A. *Nature* **1993**, 365, 141.
- (4) Aubin, S. M. J.; Wemple, M. W.; Adams, D. M.; Tsai, H.-L.; Christou, G.; Hendrickson, D. N. *J. Am. Chem. Soc.* **1996**, 118, 7746.
- (5) Boskovic, C.; Brechin, E. K.; Streib, W. E.; Folting, K.; Bollinger, J. C.; Hendrickson, D. N.; Christou, G. *J. Am. Chem. Soc.* **2002**, 124, 3725.
- (6) Friedman, J. R.; Sarachik, M. P.; Tejada, J.; Ziolo, R. *Phys. Rev. Lett.* **1996**, 76, 3830.
- (7) Thomas, L.; Lioni, L.; Ballou, R.; Gatteschi, D.; Sessoli, R.; Barbara, B. *Nature* **1996**, 383, 145.
- (8) Wernsdorfer, W.; Sessoli, R. *Science* **1999**, 284, 133.

an enveloping shell of organic groups that ensure the “magnetic cores” are not in contact and which can be varied at will by standard chemistry methods. In addition, the QTM they exhibit is advantageous for some potential applications of SMMs, for example, in providing the quantum superposition of states needed for a system to be capable of functioning as a quantum bit (qubit) for quantum computing,<sup>9</sup> but is a serious disadvantage for others, such as the storage on a single molecule of one bit of digital information, where the preferential alignment of the magnetization vector would be lost.

With the field of single-molecule magnetism now firmly established, two important questions (among many) that need to be addressed are (i) can much larger SMMs than are currently known be made and (ii) if so, will they still unequivocally demonstrate quantum properties? As part of our continuing work in the field of SMMs, we have been seeking the synthesis of such larger examples. In this paper, we report a Mn<sub>30</sub> SMM that is of the size of a small protein and which is by far the largest SMM to date. We describe its structural and magnetic characterization, and, in addition, we show that it still unambiguously exhibits QTM.

## Experimental Section

**Syntheses.** All manipulations were performed under aerobic conditions using chemicals as received, unless otherwise stated. [Mn<sub>12</sub>O<sub>12</sub>(O<sub>2</sub>CCH<sub>2</sub>Bu<sup>t</sup>)<sub>16</sub>(H<sub>2</sub>O)<sub>4</sub>] (**1**) was prepared as described previously.<sup>10</sup>

[Mn<sub>30</sub>O<sub>24</sub>(OH)<sub>8</sub>(O<sub>2</sub>CCH<sub>2</sub>Bu<sup>t</sup>)<sub>32</sub>(H<sub>2</sub>O)<sub>2</sub>(MeNO<sub>2</sub>)<sub>4</sub>] (**2**). A solution of complex **1** (0.20 g, 0.072 mmol) in CH<sub>2</sub>Cl<sub>2</sub> (50 mL) was filtered, and the filtrate was layered with MeNO<sub>2</sub> (≥50 mL). The mixture was left for several days, during which time some solvent was allowed to evaporate, and small black crystals of **2** (sometimes contaminated with **1**) were obtained. These were collected by filtration, redissolved in CH<sub>2</sub>Cl<sub>2</sub>, and relayered with MeNO<sub>2</sub>. After several days, black crystals of pure complex **2** were obtained, and these were maintained in mother liquor for X-ray crystallography and other single-crystal studies or were collected by filtration. The yield was 35%. Anal. Calcd for **2**·4CH<sub>2</sub>Cl<sub>2</sub>: C, 37.11; H, 5.98; N, 0.87. Found: C, 37.40; H, 6.03; N, 0.68.

**X-ray Crystallography.** X-ray crystallographic data were collected on a SMART 6000 (Bruker) diffractometer. A suitable crystal (approximate dimensions 0.30 × 0.25 × 0.25 mm<sup>3</sup>) was attached to the tip of a glass capillary and transferred to the goniostat, where it was cooled for characterization and data collection. A preliminary set of cell constants was calculated from reflections harvested from three sets of 20 frames. The data collection was carried out using Mo Kα radiation (graphite monochromator) with a frame time of 30 s and a detector distance of 5.0 cm. Three major sections of frames were collected with 0.30° steps in  $\omega$  at three different  $\varphi$  settings and a detector position of −43° in  $2\theta$ . The intensity data were corrected for absorption (SAD-ABS).<sup>11</sup> Final cell constants were calculated from the *xyz* centroids of 8974 strong reflections from the actual data collection after integration (SAINT).<sup>12</sup> The space group *C2/c* was determined from intensity statistics and systematic absences. The structure was solved by direct methods using SIR-92<sup>13</sup> and was refined with SHELXL-97.<sup>14</sup> Most of the non-hydrogen atoms were refined with anisotropic displacement parameters. The exceptions were the C atoms belonging to two disordered *tert*-butyl groups (C62 to C66 and C69 to C72) and Cl and C

atoms of the solvent molecules. The H atoms were placed in ideal positions and refined as riding atoms with relative isotropic displacement parameters.

The complex packs inefficiently, creating large voids in which disordered solvent is located. The *tert*-butyl groups of some ligands adjacent to the voids are disordered over two or more sites. The models for these include refinements over only two sites with fixed or refined occupancies, and an appropriate set of restraints and constraints. The thermal displacement patterns of these *tert*-butyl groups and the remaining electron density suggest that more sites may be partially occupied and/or that other ligands may occupy the site part of the time. However, the data are not sufficient to model and refine such details. The identity of some solvent molecules could be established, but a major part of the solvent present in the structure remains unmodeled.<sup>15a</sup> Taking only the volume of the Mn<sub>30</sub> complex into account, a fifth of the unit cell is solvent accessible area. It was not possible to obtain a reliable electron count in this space.<sup>15b</sup>

The final full-matrix least-squares refinement on *F*<sup>2</sup> converged to *R*1 = 0.0885 and *wR*2 = 0.3208 (*F*<sup>2</sup>, all data). The remaining electron density in a difference Fourier map was located in the vicinity of solvent molecules and disordered peripheral ligands.

**Other Studies.** Infrared spectra were recorded in the solid state (KBr pellets) on a Nicolet model 510P FTIR spectrophotometer in the 400–4000 cm<sup>−1</sup> range. Elemental analyses (C, H, and N) were performed on a Perkin-Elmer 2400 Series II Analyzer. Direct current (DC) and alternating current (AC) magnetic susceptibility studies were performed at the University of Florida on a Quantum Design MPMS-XL SQUID susceptometer equipped with a 7 T magnet and operating in the 1.8–400 K range. Samples were embedded in solid eicosane to prevent torquing. Magnetization versus field and temperature data were fit using the program MAGNET.<sup>16</sup> Pascal's constants were used to estimate the diamagnetic correction, which was subtracted from the experimental susceptibility to give the molar paramagnetic susceptibility ( $\chi_M$ ). Low-temperature (<1.8 K) hysteresis loop and DC relaxation measurements were performed at Grenoble using an array of micro-SQUIDs.<sup>17</sup> The high sensitivity of this magnetometer allows the study of single crystals of SMMs of the order of 10–500  $\mu$ m. The field can be applied in any direction by separately driving three orthogonal coils.

## Results and Discussion

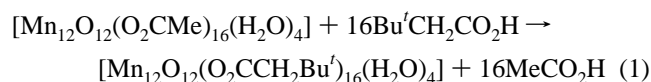
**Syntheses.** [Mn<sub>30</sub>O<sub>24</sub>(OH)<sub>8</sub>(O<sub>2</sub>CCH<sub>2</sub>Bu<sup>t</sup>)<sub>32</sub>(H<sub>2</sub>O)<sub>2</sub>(MeNO<sub>2</sub>)<sub>4</sub>] (**2**) was obtained when [Mn<sub>12</sub>O<sub>12</sub>(O<sub>2</sub>CCH<sub>2</sub>Bu<sup>t</sup>)<sub>16</sub>(H<sub>2</sub>O)<sub>4</sub>] (**1**) was recrystallized from a mixture of CH<sub>2</sub>Cl<sub>2</sub> and MeNO<sub>2</sub>. This was a surprising and, needless to say, unexpected transformation, given the successful recrystallization without change of numerous other [Mn<sub>12</sub>O<sub>12</sub>(O<sub>2</sub>CR)<sub>16</sub>(H<sub>2</sub>O)<sub>4</sub>] complexes in the past with a variety of R groups. That this unusual transformation should have occurred with **1** is, however, consistent with the fact that this particular complex had previously displayed other reactivity behavior atypical of Mn<sub>12</sub> complexes. Complex **1** can be prepared by our standard ligand substitution reaction<sup>10</sup> between [Mn<sub>12</sub>O<sub>12</sub>(O<sub>2</sub>CMe)<sub>16</sub>(H<sub>2</sub>O)<sub>4</sub>] and an excess of Bu<sup>t</sup>CH<sub>2</sub>CO<sub>2</sub>H. Final crystallization of the product, in the presence still of some Bu<sup>t</sup>CH<sub>2</sub>CO<sub>2</sub>H, from CH<sub>2</sub>Cl<sub>2</sub>/MeNO<sub>2</sub> (1:1) successfully gave black crystals of complex **1** (eq 1).

(15) (a) Initially the model included more partial solvent molecules (CH<sub>3</sub>NO<sub>2</sub> and CH<sub>2</sub>Cl<sub>2</sub>) that were placed on the basis of thermal displacement patterns of the neighboring or superimposed solvent molecules or difference maps. Such a model has lower *R*-values but fails to converge. Therefore, those partial molecules were removed until a stable model was obtained that converged. The solvent molecules reported here are real; their true site occupancy may be faulty, however, because electron density in the vicinity of the refined site may be picked up causing erroneous displacements and site occupancies. (b) PLATON: Spek, A. L. *Acta Crystallogr.* **1990**, *A46*, C34.

(16) MAGNET, Davidson, E. R., Indiana University.

(17) Wernsdorfer, W. *Adv. Chem. Phys.* **2001**, *118*, 99.

(9) Leuenberger, M. N.; Loss, D. *Nature* **2001**, *410*, 789.  
 (10) Eppley, H. J.; Tsai, H.-L.; Vries, N.; Folting, K.; Christou, G.; Hendrickson, D. J. *Am. Chem. Soc.* **1995**, *117*, 301.  
 (11) An empirical correction for absorption anisotropy: Blessing, R. *Acta Crystallogr.* **1995**, *A51*, 33.  
 (12) SAINT 6.1, Bruker Analytical X-ray Systems, Madison, WI.  
 (13) SIR92: Altomare, A.; Cascarno, G.; Giacovazzo, C.; Gualardi, A. *J. Appl. Crystallogr.* **1993**, *26*, 343.  
 (14) SHELXTL-Plus V5.10, Bruker Analytical X-ray Systems, Madison, WI.



However, on some occasions, we happened to leave the crystals in the mother liquor longer than normal (>5 days) and noticed that the crystals slowly redissolved, with the formation in their place of a small amount of lighter red-brown crystals. These were identified by their IR spectrum and unit cell determinations as  $[\text{Mn}_8\text{O}_2(\text{O}_2\text{CCH}_2\text{Bu}')_{14}(\text{HO}_2\text{CCH}_2\text{Bu}')_4]$  (**3**; 2Mn(II), 6Mn(II)). The latter was previously synthesized in our group<sup>18</sup> by a reductive destabilization in  $\text{CH}_2\text{Cl}_2/\text{MeNO}_2$  of  $[\text{Mn}_{12}\text{O}_{12}(\text{O}_2\text{CCH}_2\text{Bu}')_{16}(\text{H}_2\text{O})_4]$  with, for example, phenol. It was interesting, and subsequently of relevance to the present work, to find that (i) the conversion of **1** to **3** only occurs in the presence of  $\text{MeNO}_2$  and (ii)  $\text{Mn}_{12}$  complexes containing other carboxylate ligands (e.g.,  $\text{MeCO}_2^-$ ) did not give the corresponding  $\text{Mn}_8$  complex even in  $\text{CH}_2\text{Cl}_2/\text{MeNO}_2$ . The transformation was thus specific to  $\text{Bu}'\text{CH}_2\text{CO}_2^-$  groups and  $\text{MeNO}_2$ . Similarly, the conversion of **1** to  $\text{Mn}_{30}$  product **2** only occurs when the former is recrystallized from  $\text{CH}_2\text{Cl}_2/\text{MeNO}_2$ , but even then only if no  $\text{Bu}'\text{CH}_2\text{CO}_2\text{H}$  is present in the solution, as mentioned above; recrystallization of **1** from  $\text{CH}_2\text{Cl}_2/\text{MeNO}_2$  in the presence of  $\text{Bu}'\text{CH}_2\text{CO}_2\text{H}$  gives black crystals of **1**. Similarly, **1** can be recrystallized without change from  $\text{CH}_2\text{Cl}_2/\text{MeCN}$ .

It is very likely that a major contribution to the transformation of **1** to **2** (or **3**) is the high basicity of  $\text{Bu}'\text{CH}_2\text{CO}_2^-$ , as reflected in the relatively large  $\text{pK}_a$  value of its conjugate acid,  $\text{Bu}'\text{CH}_2\text{CO}_2\text{H}$  (5.24). The 16 strongly electron-donating carboxylate groups in **1** (average Mn oxidation state +3.33) will facilitate its transformation to **2** (average Mn oxidation state +2.93). However, the overall conversion of **1** to **2** is clearly very complicated, and it undoubtedly involves a variety of fragmentation, aggregation, and redox processes. The large bulk of  $\text{Bu}'\text{CH}_2\text{CO}_2^-$  groups and the high solubility imparted by these groups no doubt also contribute to the successful isolation and crystallization of this particular and very large molecule.

**Description of the Structure.** ORTEP representations as PovRay plots are presented in Figures 1 and 2. Selected interatomic distances are listed in Table 2.

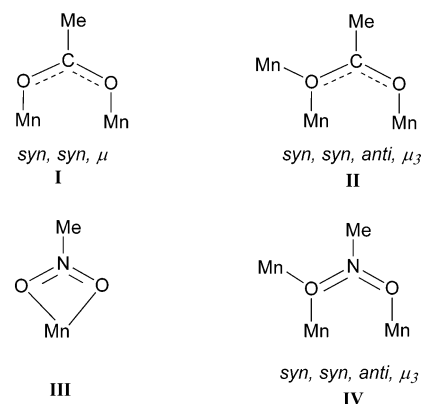
Complex  $2 \cdot x\text{CH}_2\text{Cl}_2 \cdot y\text{solvent}$  (Table 1) crystallizes in the monoclinic space group  $C2/c$  with four molecules in the unit cell. The large size and irregular shape of this molecule (volume  $\approx 7 \text{ nm}^3$ , molar mass  $\approx 6133 \text{ Da}$ ), which approaches the size of a small protein, creates voids that contain disordered solvent molecules, primarily  $\text{CH}_2\text{Cl}_2$ , and allow disorder of ligand  $\text{Bu}'$  groups adjacent to the voids. The crystal structure shows solvent/ligand sites merely as the average of all unit cells in the crystal, with some sites occupied so infrequently that they are invisible in this experiment. The structure of the  $\text{Mn}_{30}$  molecule consists of a central, near-linear  $[\text{Mn}_4\text{O}_6]$  backbone unit containing Mn atoms Mn(1), Mn(2), Mn(3), and Mn(4). This  $[\text{Mn}_4\text{O}_6]$  linear unit has never been seen in discrete form, although it is a recognizable fragment of other high-nuclearity Mn carboxylate clusters, such as the family of  $\text{Mn}_{18}$  compounds.<sup>19</sup> On either side of this central unit are two  $[\text{Mn}_{13}\text{O}_9(\text{OH})_4]$  units attached to the oxide ions of the former. Peripheral ligation around the

resulting  $[\text{Mn}_{30}\text{O}_{24}(\text{OH})_8]$  core is by 32  $\text{Bu}'\text{CH}_2\text{CO}_2^-$ , 2  $\text{H}_2\text{O}$ , and 4  $\text{MeNO}_2$  groups. The molecule has crystallographically imposed  $C_2$  symmetry with the  $C_2$  axis passing through the four Mn atoms of the central unit. All of the Mn atoms are six-coordinate with near-octahedral geometry, except for Mn(10) and Mn(16) (and their symmetry related partners), which are five-coordinate. At Mn(4), there is an unusually long  $\text{Mn}-\text{O}^{2-}$  contact ( $\text{Mn}(4)-\text{O}(4)$  and  $\text{Mn}(4)-\text{O}(4') = 2.423(6) \text{ \AA}$ ), giving a particularly distorted octahedral geometry at this site. The  $\text{OH}^-$  groups are all bridging, and the water molecules are terminally coordinated to Mn(2). The carboxylate groups are also all bridging, except for those on Mn(17) and Mn(17'), which are monodentate.

The Mn oxidation states were determined by qualitative inspection of the relative Mn–O bond distances, as well as quantitative calculation of bond valence sums (BVS). The latter are shown in Table 3. These considerations suggest that the complex is mixed- and trapped-valence, containing 1  $\text{Mn}^{4+}$ , 26  $\text{Mn}^{3+}$ , and 3  $\text{Mn}^{2+}$  ions, which are shown as different colors in Figure 1 (top). The  $\text{Mn}^{4+}$  ion is in the central  $[\text{Mn}_4\text{O}_6]$  unit, as is one of the three  $\text{Mn}^{2+}$  ions, the others being Mn(17) and Mn(17') on the extremity of the molecule. The rest of the Mn ions are all  $\text{Mn}^{3+}$ , which is consistent with the Jahn–Teller (JT) axial elongations seen for the octahedral members of this set of Mn ions, as is expected for high-spin  $d^4$  ions in this geometry.

Bond valence sum calculations were also performed for the inorganic O atoms to assess their degree of protonation and thus distinguish  $\text{O}_2^-/\text{OH}^-/\text{H}_2\text{O}$  situations. The results are listed in Table 4. There are 24  $\text{O}^{2-}$  ions bridging the metal centers. These can be separated into two types: 18 are  $\mu_3-\text{O}^{2-}$  and 6 are  $\mu_4-\text{O}^{2-}$  ions. Of the remaining O atoms, eight are  $\mu-\text{OH}^-$  groups and two are terminal water molecules. In the case of O(26), the BVS value of 0.44 is a little lower than is typical for an  $\text{OH}^-$  ion, which may be due to hydrogen-bonding contacts, but is otherwise consistent with the Mn oxidation state assignments and overall charge balance of the neutral molecule.

The 32 carboxylate groups exhibit three types of binding modes: 24 bridge two manganese ions in the common *syn,syn, $\mu$* -bridging mode (**I**), 6 are bridging three manganese ions in the *syn,syn,anti, $\mu_3$* -bridging mode (**II**), and the final 2 are bound in a monodentate fashion to  $\text{Mn}^{\text{II}}$  ions Mn(17) or Mn(17'), as mentioned earlier. Two of the four  $\text{MeNO}_2$  molecules are



chelating Mn(17) and Mn(17') in mode **III**, whereas the other two are bridging Mn(9), Mn(8), and Mn(13) in a *syn,syn,anti, $\mu_3$* -

(18) Boskovic, C.; Huffman, J. C.; Christou, G. *Chem. Commun.* **2002**, 21, 2502.  
 (19) Brechin, E. K.; Boskovic, C.; Wernsdorfer, W.; Yoo, J.; Yamaguchi, A.; Sañudo, E. C.; Concolino, T. R.; Rheingold, A. L.; Ishimoto, H.; Hendrickson, D. N.; Christou, G. *J. Am. Chem. Soc.* **2002**, 124, 9710.



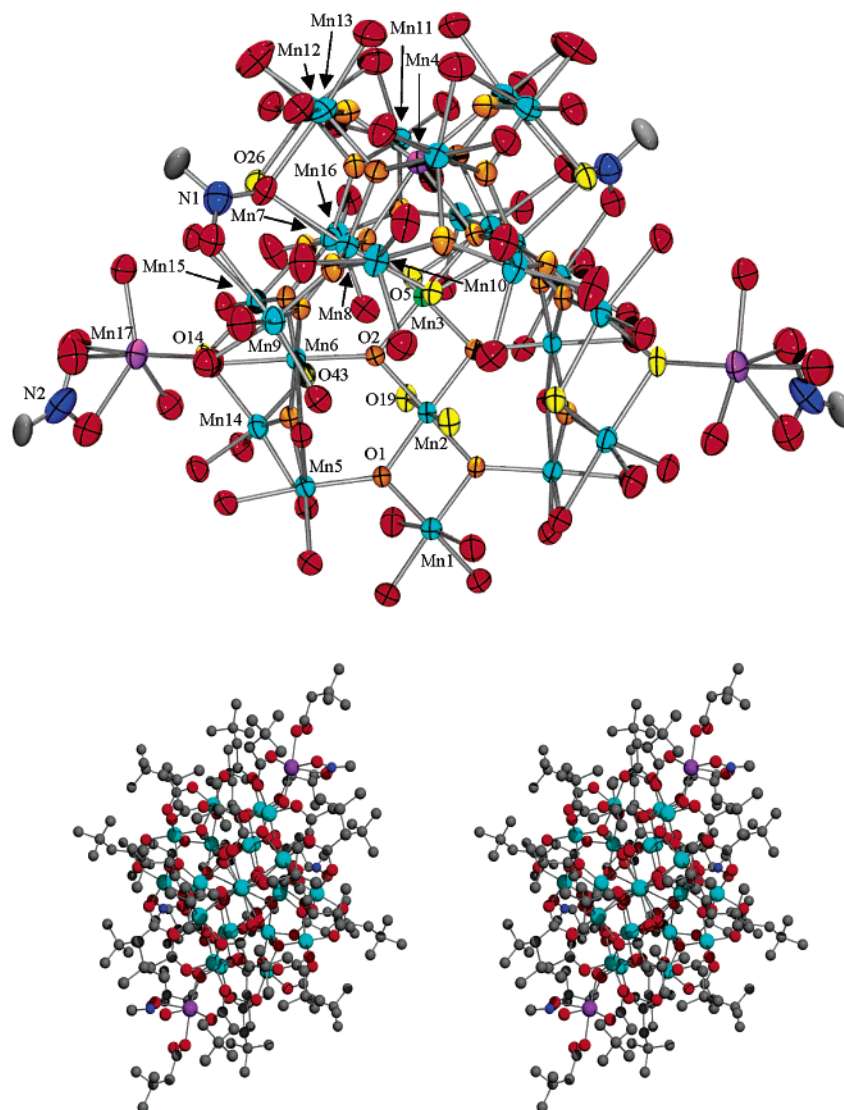


**Figure 1.** Top: Labeled ORTEP representation as a PovRay plot of complex **2** at the 50% probability level with the  $C_2$  axis vertical. For clarity, only the C atoms of MeNO<sub>2</sub> groups are shown. Mn<sup>IV</sup> green; Mn<sup>III</sup> sky-blue; Mn<sup>II</sup> purple; N blue; C gray; O red, except OH<sup>-</sup> and H<sub>2</sub>O yellow, and O<sup>2-</sup> orange. Bottom: Stereoview along the  $C_2$  axis using a ball-and-stick representation. Colors as for the top figure, except that all O atoms are red.

bridging mode (IV) on the JT elongation axes of these three Mn<sup>3+</sup> ions. Finally, the two terminal H<sub>2</sub>O molecules (O19, O19') are both bonded to Mn(2) on its JT elongation axis.

The 32 Bu' groups of the carboxylate ligands serve to essentially encapsulate the Mn/O core in a hydrocarbon sheath, as emphasized by the space-filling view in Figure 3. The hydrogen atoms have been omitted for convenience from this figure; with them also included, essentially none of the core atoms are visible, and the molecule appears as a distorted hydrocarbon ball. These Bu' groups impart great solubility to the complex in most solvents, even in toluene and to a significant extent in hexane.

The large voids between Mn<sub>30</sub> molecules in the crystal contain many disordered solvent molecules, primarily CH<sub>2</sub>Cl<sub>2</sub>, as well as some statically disordered carboxylate Bu' groups, as already mentioned. The solvent disorder is not surprising, given the large voids available and the absence of strong hydrogen bonding that might keep them in more ordered positions. This great disorder in the solvent molecules and in some of the Bu' groups does not merely impact negatively on the crystallographic

refinement of the structure, providing problems akin to protein crystallography, but has a very important effect on the magnetic properties (vide infra), which are acutely sensitive to the precise environment of an SMM molecule such as the Mn<sub>30</sub>.

**DC Magnetic Susceptibility Studies.** Each molecule of [Mn<sub>30</sub>O<sub>24</sub>(OH)<sub>8</sub>(O<sub>2</sub>CCH<sub>2</sub>Bu')<sub>32</sub>(H<sub>2</sub>O)<sub>2</sub>(MeNO<sub>2</sub>)<sub>4</sub>] (**2**) comprises a Mn/O magnetic core of volume ~2 nm<sup>3</sup> (2000 Å<sup>3</sup>), enveloped in a hydrocarbon shell ~0.5 nm (5 Å) thick, composed of carboxylate CH<sub>2</sub>Bu' groups. This essentially magnetically isolates neighboring Mn/O cores (Figure 3).

Variable-temperature DC magnetic susceptibility ( $\chi_M$ ) data were collected on powdered, microcrystalline samples of complex **2** in the 2.00–300 K range in a 5 kG (0.5 T) magnetic field. The  $\chi_M T$  value steadily decreases from 63.0 cm<sup>3</sup> K mol<sup>-1</sup> at 300 K to 14.21 cm<sup>3</sup> K mol<sup>-1</sup> at 5.0 K and then decreases rapidly at lower temperatures (Figure 4). The 300 K value is significantly less than the 93 cm<sup>3</sup> K mol<sup>-1</sup> expected if there were no interactions between the Mn ions in **2**. Thus, the data strongly suggest predominantly antiferromagnetic exchange interactions within the molecule, with a small but nonzero

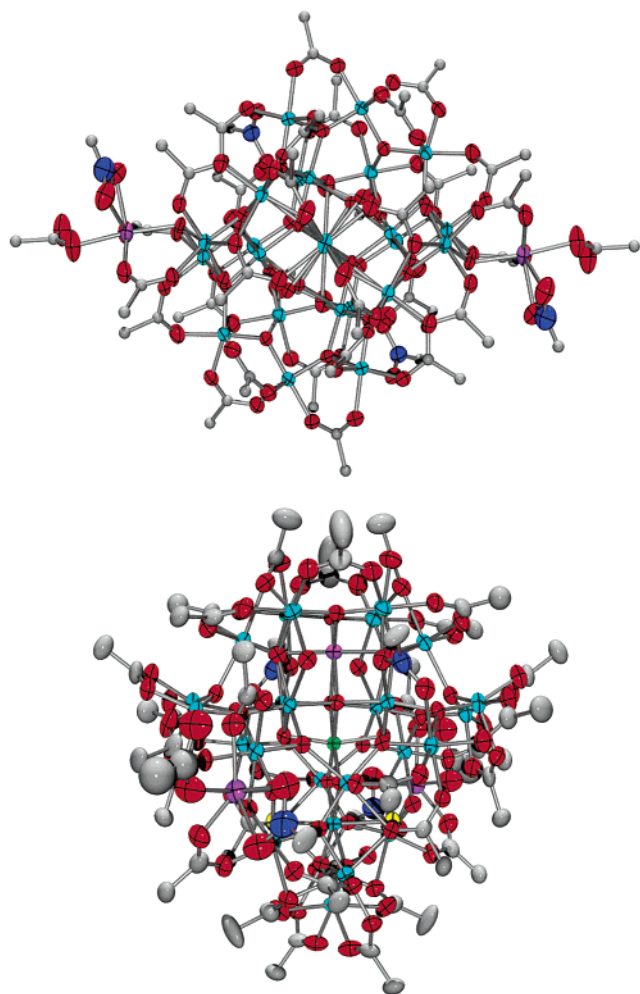


**Figure 2.** ORTEP representations as PovRay plots of complex **2** at the 50% probability level. The top and bottom figures are looking along and perpendicular to the  $C_2$  axis, respectively. For clarity, only the  $\alpha$ -C atom of each  $\text{Bu}^{\text{IV}}\text{CH}_2\text{CO}_2^-$  group is shown.  $\text{Mn}^{\text{IV}}$  green;  $\text{Mn}^{\text{III}}$  sky-blue;  $\text{Mn}^{\text{II}}$  purple; N blue; O red, except  $\text{H}_2\text{O}$  (O19 and O19') yellow; C gray.

**Table 1.** Crystallographic Data for Complex **2**· $x\text{CH}_2\text{Cl}_2$ · $y$ solvent

chemical formula <sup>a</sup>	$\text{C}_{196}\text{H}_{376}\text{Mn}_{30}\text{N}_4\text{O}_{106}$
formula wt, g/mol <sup>a</sup>	6133.39
crystal system	monoclinic
space group	$C2/c$
$a$ , Å	35.8248(11)
$b$ , Å	23.1245(11)
$c$ , Å	40.7231(16)
$\beta$ , deg	113.234(2)
volume	31 000(2) Å <sup>3</sup>
$Z$	4
$\rho_{\text{calc}}$ , g/cm <sup>3</sup>	1.357 g/cm <sup>3</sup>
$\mu$ , mm <sup>-1</sup>	1.289 mm <sup>-1</sup>
$T$ , K	113(2)
$\lambda$ , Å <sup>b</sup>	0.71073 Å
data/restraints/parameters	27 491/48/1487
GOF on $F^2$ <sup>c</sup>	1.118
final $R$ indices $[I > 2\sigma(I)]^{d,e}$	$R1 = 0.0885$ , $wR2 = 0.2718$
largest diff. peak and hole	2.471 and $-0.986$ e Å <sup>-3</sup>

<sup>a</sup> Excluding solvate molecules. <sup>b</sup> Graphite monochromator. <sup>c</sup> Goodness-of-fit =  $[\sum[w(F_o^2 - F_c^2)^2]/N_{\text{observs}} - N_{\text{params}}]^{1/2}$ , all data. <sup>d</sup>  $R1 = \sum||F_o| - |F_c||/\sum|F_o|$ . <sup>e</sup>  $wR2 = [\sum[w(F_o^2 - F_c^2)^2]/\sum[w(F_o^2)^2]]^{1/2}$ ,  $w = 1/[\sigma^2(F_o^2) + (0.2P)^2]$ , where  $P = [F_o^2 + 2F_c^2]/3$ .

ground-state spin value,  $S$ . With such a large and complicated molecule, it was clearly impossible to determine the individual pairwise exchange constants  $J_{ij}$  between  $\text{Mn}_i\text{Mn}_j$  pairs. However,

**Table 2.** Selected Interatomic Distance (Å) Ranges for Complex **2**

parameter	distances
$\text{Mn}(\text{II})\cdots\text{Mn}(\text{III})$	3.2025(15)–3.2075(15)
$\text{Mn}(\text{III})\cdots\text{Mn}(\text{III})$	2.7592(17)–3.1836(18)
$\text{Mn}(\text{III})\cdots\text{Mn}(\text{IV})$	2.850(2)–3.0308(14)
$\text{Mn}(\text{IV})-\mu_3\text{-O}^{2-}$	1.853(5)–1.948(5)
$\text{Mn}(\text{III})-\mu_3\text{-O}^{2-}$	1.805(6)–1.930(5)
$\text{Mn}(\text{III})-\mu_4\text{-O}^{2-}$	1.896(6)–1.951(5)
$\text{Mn}(\text{III})-\mu\text{-OH}^-$	1.898(6)
$\text{Mn}(\text{III})-\mu_3\text{-OH}^-$	1.966(5)
$\text{Mn}(\text{III})-\mu_3\text{-O}^{2-a}$	2.095(5)–2.138(6)
$\text{Mn}(\text{III})-\mu_3\text{-OH}^{-a}$	2.210(6)
$\text{Mn}(\text{III})-\mu\text{-OH}^{-a}$	2.258(6)–2.418(6)
$\text{Mn}(\text{III})-\text{H}_2\text{O}^a$	2.273(6)
$\text{Mn}(\text{III})-\text{O}_{\text{carb}}$	1.919(7)–2.014(5)
$\text{Mn}(\text{III})-\text{O}_{\text{carb}}^a$	2.068(7)–2.267(6)
$\text{Mn}(\text{III})-\mu\text{-O}_{\text{carb}}^{a,b}$	2.229(6)–2.347(6)
$\text{Mn}(\text{III})-\text{O}_2\text{NMe}^a$	2.364(7)–2.369(7)
$\text{Mn}(\text{II})-\mu_3\text{-O}^{2-}$	2.127(6)–2.152(6)
$\text{Mn}(\text{II})-\mu_4\text{-O}^{2-}$	2.247(5)–2.423(6)
$\text{Mn}(\text{II})-\text{O}_{\text{carb}}$	2.097(7)–2.174(7)
$\text{Mn}(\text{II})-\text{O}_{\text{carb}}^c$	2.234(8)
$\text{Mn}(\text{II})-\text{O}_2\text{NMe}$	2.281(9)–2.312(9)

<sup>a</sup> Bonds on Jahn–Teller elongation axes. <sup>b</sup> Of the  $\mu_3$ -carboxylate groups. <sup>c</sup> Of the terminal carboxylate groups.

**Table 3.** Bond Valence Sums for the Mn Atoms in Complex **2**<sup>a</sup>

atom	Mn(II)	Mn(III)	Mn(IV)	atom	Mn(II)	Mn(III)	Mn(IV)
Mn(1)	3.202057	2.92883	3.07484	Mn(10)	3.26606	2.98737	3.13630
Mn(2)	3.144866	2.87652	3.01992	Mn(11)	3.22539	2.95018	3.09725
Mn(3)	4.16624	3.81075	4.00072	Mn(12)	3.28567	3.00531	3.15513
Mn(4)	1.63326	1.49390	1.56837	Mn(13)	3.22907	2.95354	3.10078
Mn(5)	3.22734	2.95196	3.09912	Mn(14)	3.20194	2.92873	3.07473
Mn(6)	3.26345	2.98499	3.13379	Mn(15)	3.15934	2.88976	3.03382
Mn(7)	3.21460	2.94031	3.08689	Mn(16)	3.15119	2.88231	3.02599
Mn(8)	3.16776	2.89747	3.04191	Mn(17)	1.84756	1.68991	1.77416
Mn(9)	3.25233	2.97482	3.12312				

<sup>a</sup> The italic value is the one closest to the charge for which it was calculated. The oxidation state of a particular atom can be taken as the nearest whole number to the italic value.

**Table 4.** Bond Valence Sums for the Inorganic Oxygen Atoms in Complex **2**

atom	BVS	assgt <sup>a</sup>	atom	BVS	assgt <sup>a</sup>
O(1)	2.069	$\text{O}^{2-}$	O(10)	2.085	$\text{O}^{2-}$
O(2)	2.111	$\text{O}^{2-}$	O(11)	2.081	$\text{O}^{2-}$
O(3)	2.130	$\text{O}^{2-}$	O(12)	2.133	$\text{O}^{2-}$
O(4)	2.080	$\text{O}^{2-}$	O(13)	1.973	$\text{O}^{2-}$
O(5)	1.175	$\text{OH}^-$	O(14)	1.219	$\text{OH}^-$
O(6)	2.100	$\text{O}^{2-}$	O(19)	0.252	$\text{H}_2\text{O}$
O(7)	2.074	$\text{O}^{2-}$	O(26)	0.440	$\text{OH}^-$
O(8)	1.990	$\text{O}^{2-}$	O(43)	0.919	$\text{OH}^-$
O(9)	2.232	$\text{O}^{2-}$			

<sup>a</sup> The oxygen atom is an  $\text{O}^{2-}$  if the BVS is  $\sim 2$ , an  $\text{OH}^-$  if the BVS is  $\sim 1$ , and an  $\text{H}_2\text{O}$  if the BVS is  $\sim 0$ .

it was important to identify the ground-state spin of the molecule, and this was accomplished by collecting variable-temperature and variable-field magnetization ( $M$ ) data in the 1.8–4.0 K and 0.1–0.4 T ranges. The data are plotted as reduced magnetization ( $M/N\mu_B$ ) versus  $H/T$  in Figure 5. The data were fit, using the program MAGNET,<sup>16</sup> by diagonalization of the spin Hamiltonian matrix assuming only the ground state is populated, incorporating axial anisotropy ( $D\hat{S}_z^2$ ) and Zeeman terms, and employing a full powder average.<sup>20</sup> Complex **2** is

- (20) Yoo, J.; Yamaguchi, A.; Nakano, M.; Krzystek, J.; Streib, W. E.; Brunel, L.-C.; Ishimoto, H.; Christou, G.; Hendrickson, D. N. *Inorg. Chem.* **2001**, *40*, 4604.

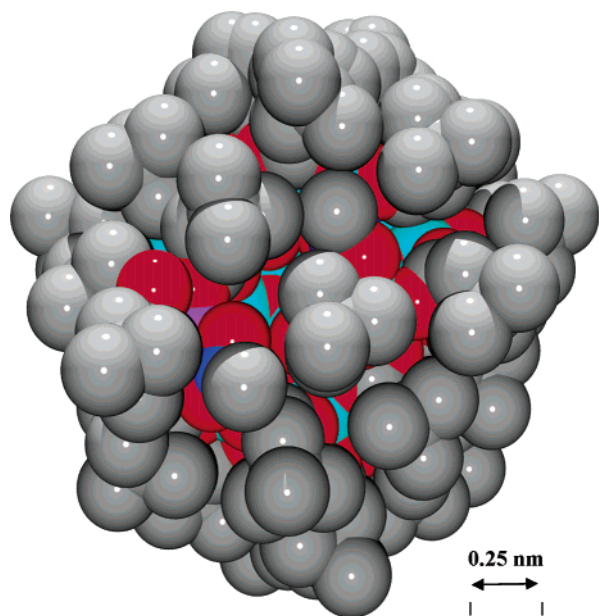


**Figure 3.** Space-filling diagram of complex **2** including all non-hydrogen atoms. The viewpoint is the same as that in Figure 2 (bottom).

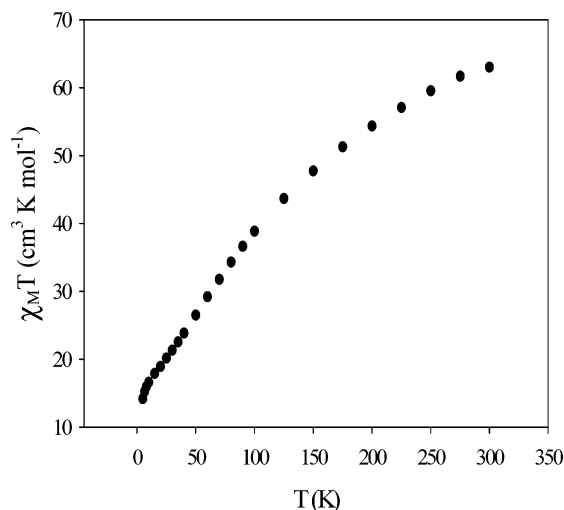


**Figure 4.** Plot of the DC magnetic susceptibility versus  $T$  for complex **2**.

thus modeled as a “giant spin” with Ising-like anisotropy. The corresponding Hamiltonian is given by eq 2,

$$\mathcal{H} = D\hat{S}_Z^2 + g\mu_B\mu_0\hat{S}_ZH_z \quad (2)$$

where  $D$  is the axial anisotropy constant,  $\mu_B$  is the Bohr magneton,  $\hat{S}_Z$  is the easy-axis spin operator,  $g$  is the electronic  $g$  factor,  $\mu_0$  is the vacuum permeability, and  $H_z$  is the applied longitudinal field. The last term in eq 2 is the Zeeman energy associated with an applied magnetic field. The fit parameters were  $S = 5$ ,  $D = -0.51 \text{ cm}^{-1}$  ( $= -0.73 \text{ K}$ ), and  $g = 2.00$ . When data collected at fields  $>15 \text{ kG}$  were included, a satisfactory fit could not be obtained, and the best fit gave an  $S > 5$  ground state. This suggests that low energy excited states with  $S > 5$  are populated, even at these relatively low temperatures. We have found that poor quality fits of the magnetization versus  $H$  and  $T$  plots are a common problem in Mn chemistry when (i) the Mn<sub>x</sub> species is of high nuclearity and there is thus a high density of spin states resulting from

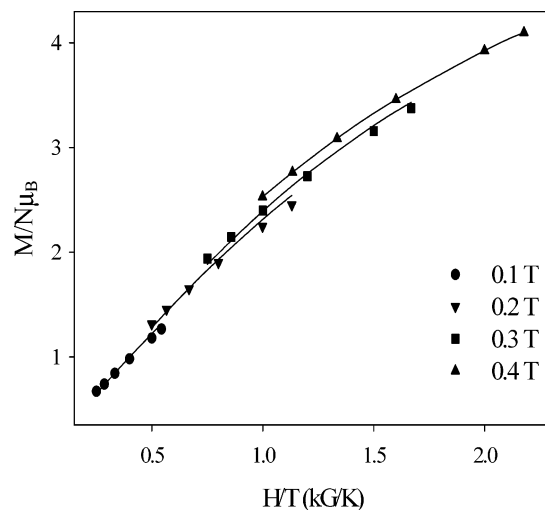


**Figure 5.** Plot of the reduced magnetization,  $M/N\mu_B$ , versus  $H/T$  for complex **2** at the indicated fields. The solid lines are the fit of the data; see the text for the fit parameters.

the exchange interactions among the many constituent Mn ions; and/or (ii) one or more Mn<sup>II</sup> ions are present, which typically give very weak (and usually antiferromagnetic) exchange interactions and thus small energy separations. As a result, there are many excited states that are low-lying (relative to  $kT$ ), and some of these will have  $S$  greater than the  $S$  of the ground state. Population of excited states will thus be difficult to avoid even at the lowest temperatures normally employed. In addition, in the presence of a big enough applied DC field,  $M_S$  components of the excited state(s) can approach in energy the lowest-lying  $M_S$  of the ground state and even cross below it. The fitting procedure assumes only a single state is occupied, and thus an  $S$  value greater than the true ground-state  $S$  is given by the best (although still poor) fit of the data because it is affected by the contributions from the populated excited state(s). As a result, we typically observe that the best fit using all of the data collected over many field values will thus overestimate the  $M$  value at low fields and underestimate the  $M$  value at large fields. For this reason, we use here for the fits only the  $M$  data collected at low fields, and a value of  $S = 5$  is obtained. Note that in the preliminary report of complex **2**, the ground state was indicated as  $S \approx 7$  due to all of the data collected in fields up to 7 T being employed in the fits.<sup>21</sup> One can also cite  $[\text{Mn}_9(\text{O}_2\text{CET})_{12}(\text{pdm})(\text{pdmH})_2(\text{L})_2]^{22}$  as an additional example, among others, of a higher nuclearity complex containing Mn<sup>II</sup> that gave problems in magnetization fits until the  $M$  data collected at higher fields were excluded.

The final  $S$  and  $D$  values obtained for complex **2** suggest an upper limit to the potential energy barrier ( $U$ ) to magnetization relaxation (reversal) of  $U = S^2|D| = 13 \text{ cm}^{-1} = 18 \text{ K}$ . This corresponds to the barrier between the lowest-lying  $M_S$  levels of the double-well potential energy plot of Figure 6. This value is large enough to suggest that complex **2** might exhibit, at sufficiently low temperatures, the slow magnetization relaxation rates characteristic of a SMM; if so, it would be the largest size SMM to be discovered to date. This was therefore investigated using AC magnetic susceptibility.

(21) Soler, M.; Rumberger, E.; Folting, K.; Hendrickson, D. N.; Christou, G. *Polyhedron* **2001**, *20*, 1365.

(22) Boskovic, C.; Wernsdorfer, W.; Folting, K.; Huffman, J. C.; Hendrickson, D. N.; Christou, G. *Inorg. Chem.* **2002**, *41*, 5107.



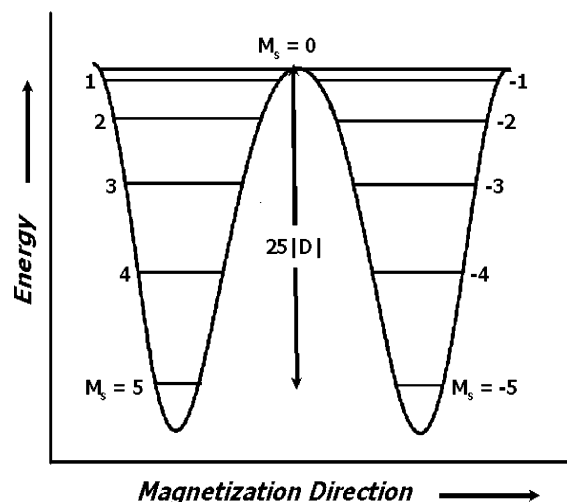


**Figure 6.** Plot of the double-well potential energy for an  $S = 5$  species such as complex **2**. The barrier to relaxation from the lowest-lying  $M_S = \pm 5$  level on one side to that on the other side is given by  $S^2|D|$ .

**AC Magnetic Susceptibility Studies.** In an AC susceptibility experiment, a weak field (typically 1–5 G) oscillating at a particular frequency ( $\nu$ ) is applied to a sample to probe the dynamics of the magnetization (magnetic moment) relaxation. An out-of-phase AC susceptibility signal ( $\chi_M''$ ) is observed when the rate at which the magnetization of a molecule relaxes is close to the operating frequency of the AC field. At low enough temperature, where the thermal energy is lower than the barrier for relaxation, the magnetization of the molecule cannot relax fast enough to keep in-phase with the oscillating field. Therefore, the molecule will exhibit a frequency-dependent  $\chi_M''$  signal indicative of slow magnetization relaxation. Frequency-dependent  $\chi_M''$  signals are an important indicator of SMMs. Further, the positions of the  $\chi_M''$  peak maxima at different AC frequencies can be used to obtain relaxation rate versus  $T$  data that can in turn yield the effective energy barrier ( $U_{\text{eff}}$ ) for the magnetization relaxation.

AC studies were performed in the 1.8–7.0 K range in a zero DC field and a 3.5 G AC field oscillating at frequencies in the 50–997 Hz range. The obtained results for three frequencies are shown in Figure 7. At temperatures below 3 K, a nonzero  $\chi_M''$  signal is observed, and this is frequency-dependent. Clearly, the peak maxima of these signals lie at temperatures  $< 1.8$  K, the operating minimum of our SQUID instrument, and cannot be observed, but the data do suggest that complex **2** does indeed display the slow magnetization relaxation dynamics of a SMM. However, confirmation of this and a detailed study of the relaxation rates required measurements at  $T < 1.8$  K.

**Hysteresis Studies below 1.8 K.** To establish whether **2** is a SMM, magnetization versus applied DC field data were collected on single crystals (that had been kept in contact with mother liquor) using a micro-SQUID apparatus. Shown in Figure 8 are the magnetization responses at DC field sweep rates of 0.14 and 0.008 T/s with the field approximately along the easy axis ( $z$  axis) of the molecule. Hysteresis loops were observed, whose coercivities (widths) increase with decreasing temperature and increasing sweep rate, as expected for the superparamagnet-like properties of a SMM. Hysteresis in magnetization versus field sweeps is the classical property of a magnet, and such loops are a diagnostic feature also of SMMs and superparamagnets below their blocking temperature ( $T_B$ ). The data thus

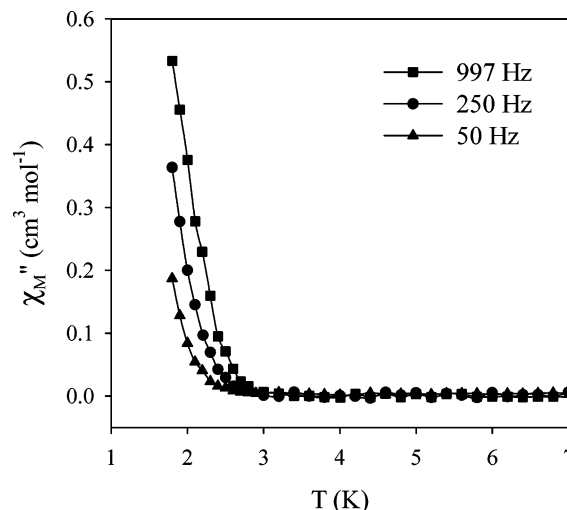


**Figure 7.** Plot of out-of-phase AC magnetic susceptibility ( $\chi_M''$ ) versus  $T$  for complex **2** at the indicated AC frequencies. The solid lines are visual aids.

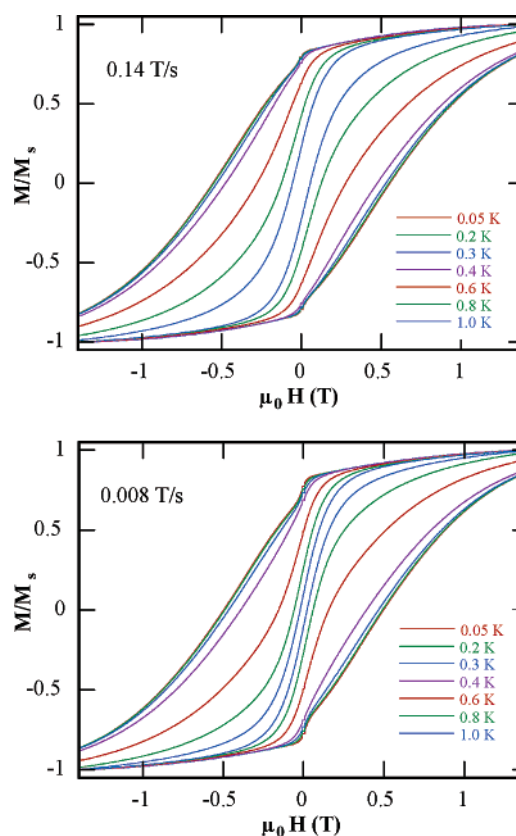


**Figure 8.** Magnetization ( $M$ ) versus DC field hysteresis loops for complex **2** at the indicated field scan rates and temperatures. The magnetization is normalized to its saturation value,  $M_S$ .

indicate complex **2** to be a new addition to the family of SMMs, the largest member (in terms of size) to date. The blocking temperature ( $T_B$ ) is  $\sim 1.4$  K, above which there is no hysteresis; that is, the spin relaxes faster to equilibrium than the time scale of the hysteresis loop measurement.

For several other SMMs studied to date, the hysteresis loops have not been smooth but have instead displayed steplike features at periodic field values.<sup>6,7,23–25</sup> These steps correspond

(23) Wernsdorfer, W.; Aliaga-Alcalde, N.; Hendrickson, D. N.; Christou, G. *Nature* **2002**, 416, 406.



to positions of increased magnetization relaxation rates and are due to quantum tunneling of the magnetization (QTM) through the anisotropy energy barrier.<sup>1</sup> The loops in Figure 8 do not show such periodic steps, although there seems to be one step just barely visible at zero field. It was suspected that complex **2** does in fact exhibit QTM but that the steps have been broadened to the point that they are smeared out and thus not visible. If so, the most likely reason is that there is a distribution of energy barriers to relaxation, that is, a distribution in  $D$  values; the separation between steps is directly proportional to  $D$ , so a distribution in  $D$  would give a distribution in step positions. Such a distribution in  $D$  values is, in fact, consistent with the crystallographically observed disorder in the solvent molecules and some carboxylate groups. In effect, the local environments around the Mn<sub>30</sub> molecules vary as a result of these disorders, altering the value of  $D$ . It should be noted that, although such disorder in solvents and ligand position might at first glance appear to be too trivial to cause a noticeable variation in the molecular  $D$  value, there is ample precedent that this is not the case. Instead, on several occasions, we have observed that such properties of SMMs are acutely sensitive to relatively small changes in the local environments of the molecules. An extreme case is the [Mn<sub>12</sub>O<sub>12</sub>(O<sub>2</sub>CCHCl<sub>2</sub>)<sub>16</sub>(H<sub>2</sub>O)<sub>4</sub>]<sup>2-</sup> anion, which has a  $D$  value of  $-0.17$  and  $-0.28$  cm<sup>-1</sup> in triclinic (PPh<sub>4</sub>)<sub>2</sub>[Mn<sub>12</sub>O<sub>12</sub>(O<sub>2</sub>CCHCl<sub>2</sub>)<sub>16</sub>(H<sub>2</sub>O)<sub>4</sub>]·4CH<sub>2</sub>Cl<sub>2</sub>·H<sub>2</sub>O and monoclinic (PPh<sub>4</sub>)<sub>2</sub>[Mn<sub>12</sub>O<sub>12</sub>(O<sub>2</sub>CCHCl<sub>2</sub>)<sub>16</sub>(H<sub>2</sub>O)<sub>4</sub>]·6CH<sub>2</sub>Cl<sub>2</sub>, respectively.<sup>25</sup> Even though the structure of the dianion is essentially superimposable in the two crystal forms, the  $D$  value differs by ~60% due to the different local symmetry in the two different space groups. In complex **2**, the large voids between molecules lead to extensive disorder and thus a distribution of molecular environments and  $D$  values. The spread in  $D$  values is clearly not expected to be as great as in the [Mn<sub>12</sub>O<sub>12</sub>(O<sub>2</sub>CCHCl<sub>2</sub>)<sub>16</sub>(H<sub>2</sub>O)<sub>4</sub>]<sup>2-</sup> anion mentioned above, but neither will it be insignificant. The same smearing out of steps was also seen in a [Mn<sub>18</sub>]<sup>2+</sup> complex, and this was similarly assigned to a distribution in  $D$  values.<sup>19,26</sup> Also, note that in real crystals there is no such thing as perfect order, and there will therefore be additional contributions to  $D$  value distributions arising from impurities, vacancies, mosaicity, and other defects.

The above discussion suggests a reason QTM steps are not seen, assuming that QTM is indeed occurring for this SMM. Yet the possibility of quantum tunneling effects still being operative in such a large molecule is of significant interest and importance, particularly for potential applications such as information storage and quantum computing, and we thus sought

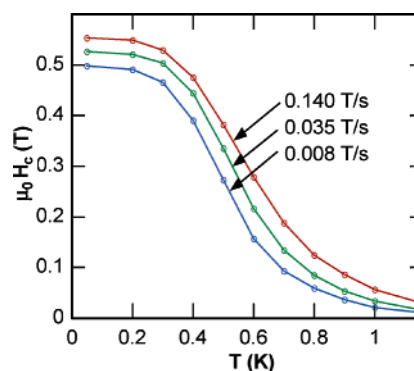


**Figure 9.** Plot of coercive field ( $H_c$ ) versus  $T$  for complex **2** at the indicated field sweep rates.

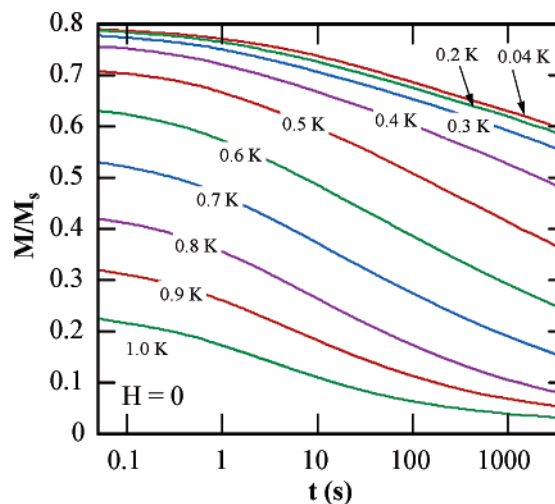


**Figure 10.** Magnetization ( $M$ ) versus time decay plots in zero DC field for complex **2**. The magnetization is normalized to its saturation value,  $M_s$ .

direct evidence for its presence, rather than merely rationalizing the absence of evidence for it in the hysteresis loops.

Although steps are not clearly visible in the hysteresis loops, they nevertheless provide other evidence of QTM. Below 0.3 K, the loops become temperature-independent, but a scan rate study shows that the loops are still time-dependent. This is illustrated in Figure 9, where the coercive field (half the width of the hysteresis loop at  $M/M_s = 0$ ) is plotted as a function of temperature. Below ~0.3 K, the coercive field is  $T$ -independent at a given scan rate, but scan-rate (i.e., time)-dependent at a given  $T$ . This is supportive of QTM from the ground-state  $M_s = -5$  of the  $S = 5$  spin manifold to  $M_s < 5$  levels on the other side of the potential double well. We will return to this point later.

An alternative way of assessing whether QTM is occurring is to monitor the decay of the magnetization with time. The sample's magnetization was first saturated in one direction at ~5 K with a large applied DC field, the temperature was then decreased to a chosen value, and then the field was removed and the magnetization decay was monitored with time. The results are shown in Figure 10 for the 0.04–1.0 K range. This provided magnetization relaxation rate ( $\Gamma$ ) versus temperature data, shown as an Arrhenius plot in Figure 11, based on the Arrhenius relationship of eq 3, where  $1/\tau_0$  is the preexponential

$$\Gamma = (1/\tau_0) \exp(-U_{\text{eff}}/kT) \quad (3)$$

- (24) (a) Tejada, J.; Ziolo, R. F.; Zhang, X. X. *Chem. Mater.* **1996**, *8*, 1784. (b) Ruiz, D.; Sun, Z.; Albela, B.; Foltting, K.; Christou, G.; Hendrickson, D. N. *Angew. Chem., Int. Ed.* **1998**, *300*. (c) Hendrickson, D. N.; Christou, G.; Ishimoto, H.; Yoo, J.; Brechin, E. K.; Yamaguchi, A.; Rumberger, E. M.; Aubin, S. M. J.; Sun, Z.; Aromi, G. *Polyhedron* **2001**, *20*, 1479. (d) Aubin, S. M.; Gilley, N. R.; Pardi, L.; Krzystek, J.; Wemple, M. W.; Brunel, L. C.; Marple, M. B.; Christou, G.; Hendrickson, D. N. *J. Am. Chem. Soc.* **1998**, *120*, 4991. (e) Yang, E.-C.; Harden, N.; Wernsdorfer, W.; Zakharov, L.; Brechin, E. K.; Rheingold, A. L.; Christou, G.; Hendrickson, D. N. *Polyhedron* **2003**, *22*, 1857. (f) Brechin, E. K.; Soler, M.; Christou, G.; Davidson, J.; Hendrickson, D. N.; Parsons, S.; Wernsdorfer, W. *Polyhedron* **2003**, *22*, 1771.
- (25) (a) Soler, M.; Wernsdorfer, W.; Abboud, K. A.; Huffman, J. C.; Davidson, E. R.; Hendrickson, D. N.; Christou, G. *J. Am. Chem. Soc.* **2003**, *125*, 3585. (b) Soler, M.; Wernsdorfer, W.; Abboud, K. A.; Hendrickson, D. N.; Christou, G. *Polyhedron* **2003**, *22*, 1777.
- (26) Sanudo, E. C.; Brechin, E. K.; Boskovic, C.; Wernsdorfer, W.; Yoo, J.; Yamaguchi, A.; Concolino, T. R.; Abboud, K. A.; Rheingold, A. L.; Ishimoto, H.; Hendrickson, D. N.; Christou, G. *Polyhedron* **2003**, *22*, 2267.

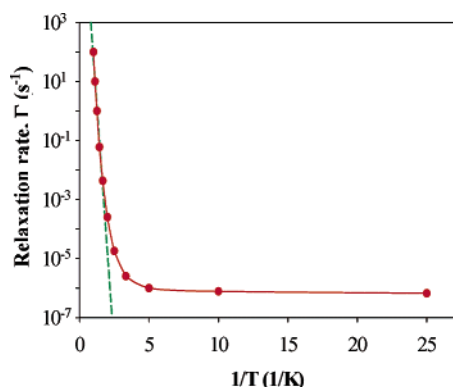


**Figure 11.** Arrhenius plot of the relaxation rate ( $\Gamma$ ) versus  $1/T$  for complex **2** using data obtained from DC magnetization decay measurements. The dashed line is the fit of the data in the thermally activated region to the Arrhenius equation; see the text for the fit parameters.

factor,  $U_{\text{eff}}$  is the mean effective barrier to relaxation, and  $k$  is the Boltzmann constant. The fit of the thermally activated region above  $\sim 0.5$  K, shown as the dashed line in Figure 11, gave  $U_{\text{eff}}/k = 15$  K and  $1/\tau_0 = 1.5 \times 10^8 \text{ s}^{-1}$ . The mean barrier  $U_{\text{eff}}$  is smaller than the calculated  $U = S^2|D| = 18$  K, as expected for QTM between higher energy  $M_S$  levels of the  $S = 5$  manifold (Figure 6). In other words, the system does not have to get to the top of the barrier (i.e., the  $M_S = 0$  level), but instead can tunnel through the barrier from some lower  $M_S$  level. At 0.2 K and below, the relaxation rate becomes temperature-independent at  $\sim 10^{-6} \text{ s}^{-1}$ . This is diagnostic of ground-state QTM; in other words, tunneling is now only between the lowest-energy  $M_S = \pm 5$  levels, and no longer via a thermally (phonon) assisted pathway involving higher-energy  $M_S$  levels. The crossover temperature between thermally activated relaxation and ground-state tunneling is between 0.2 and 0.3 K.

The ground-state tunneling deduced from the  $T$ -independent relaxation in Figure 11 also now rationalizes the one step seen at zero field in the hysteresis loops of Figure 8 at  $T < 0.3$  K. Because at these temperatures the tunneling is now only via the lowest-energy  $M_S$  levels, the distribution of  $D$  values (and thus the energy gaps to other  $M_S$  levels) no longer has such a large broadening effect on the step at zero field, and a better defined feature is thus seen.

Additional, independent confirmation of QTM in complex **2** was obtained from “quantum hole digging”.<sup>27,28</sup> This is a relatively new method that can, among other things, establish whether resonant tunneling occurs even when steps are absent in hysteresis loops due to a distribution of energy barriers. The method is based on the simple idea that after a rapid field change, the resulting magnetization relaxation at short time periods is directly related to the number of molecules in resonance at the applied field; Prokof'ev and Stamp proposed that this short time relaxation should follow a  $\sqrt{t}$  ( $t$  = time) relaxation law.<sup>29</sup> Thus, the magnetization of the molecules in the crystal was first saturated with a large negative field, and then a “digging field” ( $H_{\text{dig}}$ ) of 0.275 T was applied at 0.04 K for a chosen “digging time” ( $t_{\text{dig}}$ ). If QTM can occur, then that fraction (and only that fraction) of the molecules that is in

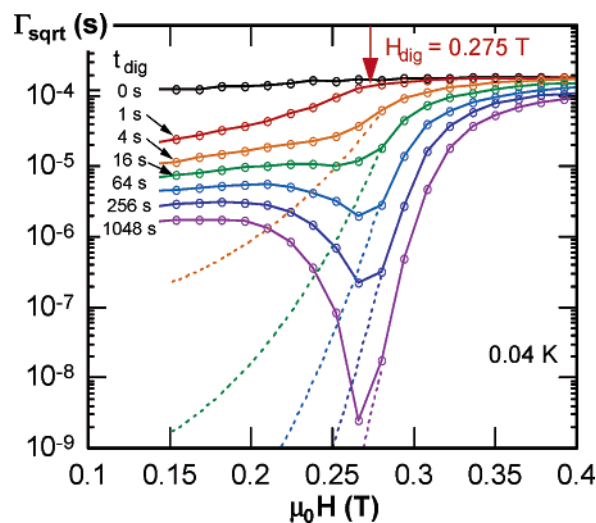


**Figure 12.** Short-time relaxation rate ( $\Gamma_{\text{sqr}}$ ) versus applied field for complex **2** measured after the sample was maintained at the applied (“digging”) field ( $H_{\text{dig}} = 0.275$  T) for different waiting (digging) times. The sharp dip (“hole”) at the digging field shows the depletion of spins that were in resonance at  $H_{\text{dig}}$ . The half-width of the hole of  $\sim 20$  mT is larger than the hyperfine field ( $\sim 10$  mT), showing the influence of dipolar couplings.

resonance at  $H_{\text{dig}}$  can undergo magnetization tunneling. In other words, only those molecules whose  $D$  values are such that at 0.275 T the  $M_S = -5$  level on one side of the barrier is equal in energy with an  $M_S$  level on the other side of the barrier can undergo a tunneling event. After  $t_{\text{dig}}$ , a field  $H_{\text{probe}}$  was applied, and the magnetization relaxation rate was measured for short time periods; from this was calculated the short-time relaxation rate ( $\Gamma_{\text{sqr}}$ ), which is related to the number of molecules still available for QTM.<sup>18</sup> The latter step is then repeated at other  $H_{\text{probe}}$  fields. The resulting plot of  $\Gamma_{\text{sqr}}$  versus  $H_{\text{probe}}$  will reflect the distribution of spins still available for tunneling after  $t_{\text{dig}}$ , and it will show a “hole” if QTM did indeed occur during the application of  $H_{\text{dig}}$  for time  $t_{\text{dig}}$  because the latter depleted from the population those spins in resonance at  $H_{\text{dig}}$ . The obtained plot for complex **2** is shown in Figure 12, and it does show a hole in this distribution. This thus supports the occurrence of QTM in the complex. Note that a classical system, or a quantum system with such a high density of states that it approaches a classical system, will not show a “quantum hole” but instead a depletion from the population of all spins with low barriers. In such a case, the  $\Gamma_{\text{sqr}}$  versus  $H_{\text{probe}}$  plot after application of  $H_{\text{dig}}$  will be given by the dashed lines in Figure 12.

The above results unequivocally establish that complex **2** undergoes resonant QTM. Of the three diagnostic tests for QTM,  $\text{Mn}_{30}$  clearly demonstrates two of them, temperature-independent relaxation and quantum hole digging. The third is steps in hysteresis loops, but these are broadened beyond resolution by the distribution of barriers ( $D$  values) resulting from a distribution of  $\text{Mn}_{30}$  environments, except for the one at zero field, which is just visible.  $\text{Mn}_{30}$  thus represents both the largest size SMM prepared to date and consequently the largest also to demonstrate QTM. To provide some size calibration, we compare in Figure 13 the Mn/O core of complex **2** with those of the  $\text{Mn}_4$  and  $\text{Mn}_{12}$  SMMs, which have been well studied to date; the  $\text{Mn}_{30}$  core is significantly larger in size.

The observation of quantum tunneling in such a large species is of relevance to the general question of whether quantum effects can still be seen in entities whose size is much larger

(27) Wernsdorfer, W.; Ohm, T.; Sangregorio, C.; Sessoli, R.; Mailly, D.; Paulsen, C. *Phys. Rev. Lett.* **1999**, *82*, 3903.

(28) Wernsdorfer, W.; Caneschi, A.; Sessoli, R.; Gatteschi, D.; Cornia, A.; Villari, V.; Paulsen, C. *Phys. Rev. Lett.* **2000**, *84*, 2965.

(29) Prokof'ev, N. V.; Stamp, P. C. E. *Phys. Rev. Lett.* **1998**, *80*, 5794.

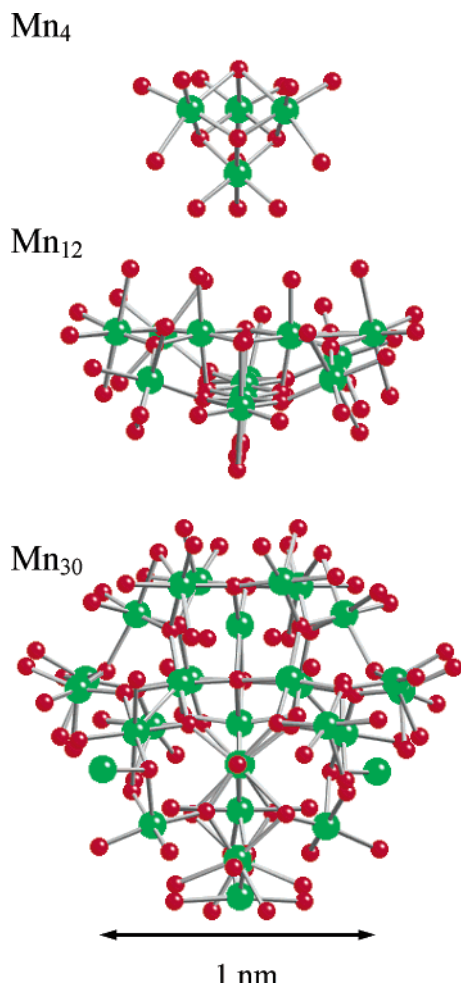


**Figure 13.** Comparison of the size of the Mn/O core of complex **2** with those of the Mn<sub>4</sub> and Mn<sub>12</sub> single-molecule magnets. Color code: Mn green, O red.

than the microscale at which quantum effects are normally observed. The reported data establish that quantum effects in Mn<sub>30</sub> can be clearly observed even in very large “magnetic particles”, significantly larger than the Mn<sub>12</sub> species. It should be pointed out that the spin  $S = 5$  of complex **2**, which is relatively small, merely represents the net uncompensated spin in the molecule and is useful as a tracer with which to monitor quantum tunneling. This  $S = 5$  tracer spin is, however, merely the uncompensated resultant of a large number of interacting electrons involved in the tunneling event. Not only the total of 122 unpaired d-electrons from the Mn ions must be considered, but also the paired electrons on the bridging O atoms through which the superexchange interaction is transmitted. In effect, there are several hundred interacting electrons within the Mn/O core that can be considered to be involved in the tunneling event. In fact, along these lines, an alternative way of comparing spin systems undergoing tunneling, and one often used for classical nanomagnetic particles,<sup>30</sup> is to use the magnitude of the Néel

vector. This is the sum of the single-ion spins of the constituent metal ions. The Néel vector for Mn<sub>30</sub> is 61, which may be compared to much smaller values of 22, 20, and 7.5 for the Mn<sub>12</sub>, Fe<sub>8</sub>, and Mn<sub>4</sub> SMMs, respectively.

The ability to observe QTM in Mn<sub>30</sub> is directly the result of the latter’s monodisperse nature and highly ordered arrangement within the crystal, notwithstanding the solvent and Bu’ disorder, which in an absolute sense is a small perturbation. This is one of the main advantages of a molecular approach to nanoscale magnetic materials, some others being room-temperature solution synthesis, true solubility (rather than colloidal suspension) in common organic solvents, and an insulating shell of organic groups around the magnetic core, which additionally can be varied at will using standard synthetic chemistry methods. These factors prevent complications from distributions of particle size, shape, surface roughness, and spin. The latter have hampered previous attempts to clearly establish QTM in large magnetic particles, both for classical magnetic materials such as Co metal and for molecules such as the ferritin protein.<sup>17,31</sup> In this regard, the hydrocarbon shell of organic groups in Mn<sub>30</sub> is particularly important, because any surface effects, such as intermolecular contacts, positional disorder of surface groups, disorder in the solvent molecules, and their hydrogen bonding to the molecule, etc., do not directly impinge significantly upon the Mn/O cores, and thus the latter are essentially identical in every molecule. This hydrocarbon shell thus essentially provides diamagnetic insulation between the magnetic cores. Of course, there are instances where intermolecular interactions between the magnetic cores are desirable, such as in the recently discovered exchange-biasing of QTM in SMMs;<sup>23</sup> in these cases, the synthetic manipulation that is possible of the organic groups about the core is also important.

Finally, we comment that Mn<sub>30</sub> represents proof-of-feasibility of extending the single-molecule magnetism phenomenon to much larger species than those in which it was discovered. There seems no reason that even larger size SMMs should not be amenable to synthesis. In this sense, the molecular or “bottom-up” approach can conceivably approach in the not-too-distant future the size regime of the “top-down”, or classical approach, to nanoscale magnetic materials and still bring with it the advantages mentioned above.

**Acknowledgment.** We thank the National Science Foundation for support of this work.

**Supporting Information Available:** An X-ray crystallographic file in CIF format for complex **2**·xCH<sub>2</sub>Cl<sub>2</sub>·ysolvent. This material is available free of charge via the Internet at <http://pubs.acs.org>.

JA0297638

(30) Lu, R.; von Delft, J. *Phys. Rev. B* **2003**, 67, 104425.

(31) (a) Awschalom, D. D.; Smyth, J. F.; Grinstein, G.; DiVincenzo, D. P.; Loss, D. *Phys. Rev. Lett.* **1992**, 68, 3092. (b) Gider, S.; Awschalom, D. D.; Douglas, T.; Mann, S.; Chaparala, M. *Science* **1995**, 268, 77. (c) Tejada, J. *Science* **1996**, 272, 424. (d) Mamiya, H.; Nakatani, I.; Furubayashi, T. *Phys. Rev. Lett.* **2002**, 88, 067201. (e) Wernsdorfer, W.; Bonet Oroscio, E.; Hasselbach, K.; Benoit, A.; Maily, D.; Kubo, O.; Nakano, H.; Barbara, B. *Phys. Rev. Lett.* **1997**, 79, 4014.